Crystal structure, spin flop transition, and magnetoelectric effect in the honeycomb-lattice frustrated Fe-doped $Ni_2Mo_3O_8$ antiferromagnets

Zhipeng Yu,[1,2] Hao Ding,[1] Kun Zhai,[1,*] Congpu Mu,[1,†] Anmin Nie,[1] Junzhuang Cong,[3] Junquan Huang,[1] Houjian Zhou,[1] Qingkai Wang,[1] Fusheng Wen,[1] Jianyong Xiang,[1] Bochong Wang,[1] Tianyu Xue,[1] Zhongming Zeng,[2] and Zhongyuan Liu[1]

[1]*Center for High Pressure Science (CHiPS), State Key Laboratory of Metastable Materials Science and Technology, Yanshan University, Qinhuangdao 066004, China*

[2]*Nanofabrication facility, Suzhou Institute of Nano-Tech and Nano-Bionics, Chinese Academy of Sciences, Suzhou 215123, China*

[3]*Beijing National Laboratory for Condensed Matter Physics, Institute of Physics, Chinese Academy of Sciences, Beijing 100049, China*

(Received 3 November 2023; revised 25 December 2023; accepted 4 January 2024; published 31 January 2024)

The magnetoelectric (ME) effect, with the cross coupling between magnetism and electric polarization, provides a new controlling dimension for creating novel information storage devices. Here, we report crystal structure, magnetic field-induced spin flop transition, and ME behaviors of Fe-doped $Ni_2Mo_3O_8$ by using comprehensive characterization methods of x-ray diffraction, high-angle annular dark-field images, magnetization, specific-heat capacity, dielectric and electric polarization measurements. The Fe/Ni honeycomb lattice is endowed with strong magnetic frustration. Through Fe doping, a metamagnetic spin flop (SF) transition and the related linear magnetoelectric effect are achieved under a lower magnetic field, which is due to the delicate modification of magnetic interactions. Consequently, the maximum direct ME coefficient α_H ($=238\,ps\,m^{-1}$) and converse ME coefficient α_E ($=110\,ps\,m^{-1}$) were achieved in $Ni_{0.5}Fe_{1.5}Mo_3O_8$ at the phase boundary of antiferromagnetic-SF and SF phase, respectively.

DOI: 10.1103/PhysRevB.109.024442

I. INTRODUCTION

Multiferroic materials with the coexistence and cross coupling of ferromagnetic (antiferromagnetic) and ferroelectric (antiferroelectric) orders could provide possibilities for constructing novel spintronic devices [1–10]. However, magnetoelectric (ME) effect exists in very finite materials from the viewpoint of the symmetry constraint [11]. Nevertheless, the microscopic mechanism of spin-induced polarization [11], such as spin-current model [12], spin-dependent d-p hybridization model [13–15], and exchange striction [16–18], stimulates the search for the multiferroic materials with collinear (E-type antiferromagnetic) or noncollinear magnetic structure.

Recently, intensive efforts have been focused on the ME properties in frustrated magnets due to their intrinsic noncollinear spin arrangement. Some materials present unique polarization responses along with the occurrence of metamagnetic transition (e.g., spin flop, magnetization plateau) in the trigonal, kagome, or honeycomb lattice, such as Ni_3TeO_6 [19], $Ni_3V_2O_8$ [20], $KCuF_3$ [21], $Co_4Nb_2O_9$ [22], and $M_2Mo_3O_8$ [23] (M = Fe, Mn, Ni, etc.). In order to achieve a greater magnetoelectric coupling, magnetoelectric materials need further improvements in design. The chemical doping is a promising method to achieve the modification of ME materials. For example, in $Ca_2Fe_{2-x}Al_xO_5$ ($0.6 \leqslant x \leqslant 1$) single crystals, the spin easy axis varies from the c axis to the a axis with increasing Al content. When magnetic field is applied along the spin easy axis, a spin flop transition takes place, accompanied by anomalies in the electric polarization and dielectric constant [24]. The family of $M_2Mo_3O_8$ (M: Mn, Fe, Co, Ni, etc.) also constitutes a magnetic frustrated system, where diverse magnetic phases exist in a delicate balance of magnetic exchange interactions. The balance may be disrupted by chemical doping effect on specific magnetic sites, allowing for tunable ME effects. For instance, increasing Zn amount in $Fe_{2-x}Zn_xMo_3O_8$ stabilizes the spontaneous ferrimagnetic state [25,26], Fe-doped $Mn_2Mo_3O_8$ achieves a large variation in a diagonal component of the linear magnetoelectric susceptibility [27], Mg-doped $Fe_2Mo_3O_8$ enhances linear and second-order magnetoelectric effect [28], and Mg-doped $Ni_2Mo_3O_8$ induces the weak ferromagnetic state [29]. $Ni_2Mo_3O_8$ shares stripy and zigzag non-Néel antiferromagnetic (AFM) orders with noncentrosymmetric $S = 1$ honeycomb lattice [30]. The strong spin frustration suppresses the long-range magnetic ordering of the Néel state, causing the low antiferroelectric temperature of $Ni_2Mo_3O_8$ and high magnetic field of spin flop transition.

Here, Fe-doped $Ni_2Mo_3O_8$ has been synthetized and its crystal structure, antiferromagnetic order, and magnetoelectric behaviors have been systematically investigated. The substitution of Fe^{2+} for Ni^{2+} not only caused a significant increase in the antiferromagnetic temperature and a substantial decrease in the magnetic field of spin flop transition but also greatly enhanced the ME effect.

II. EXPERIMENTAL DETAILS

As shown in Supplemental Material, Fig. S1(a) [31], the growth of single crystals of $Ni_{2-x}Fe_xMo_3O_8$ ($x = 0$, 0.5, 1.0, 1.5, and 2.0) was conducted in a horizontal two-zone tube furnace using the chemical vapor transport method with $TeCl_4$

*kunzhai@ysu.edu.cn
†congpumu@ysu.edu.cn

as the transport agent [32]. The mixture of Fe (99.9%, Alfa Aesar), Fe_2O_3 (99.9%, Alfa Aesar), NiO (99.9%, Alfa Aesar), and MoO_2 (99.9%, Alfa Aesar) was weighed by amounts of the desired stoichiometric ratio and thoroughly grounded before being placed into a quartz ampoule. The experimental temperature vs time is shown in Fig. S1(b) and Table S1 [31].

The x-ray diffraction of the *ab* plane was measured by an x-ray diffractometer (Smartlab, Rigaku) at room temperature. Transmission electron microscope (TEM) measurements were conducted at 300 kV by applying an aberration-corrected FEI Themis Z scanning transmission electron microscopy (STEM) equipped with a four-detector energy-dispersive x-ray spectroscope (EDS). The magnetization of samples was measured at a physical property measurement system (PPMS) (EverCool II, Quantum Design) equipped with vibrating sample magnetometer (VSM). The electric-field modulation of magnetization was examined by using a homemade VSM sample holder with a high-resistance electrometer (6517B, Keithley) providing external voltage. The PPMS relaxation calorimeter was used to measure the heat capacity. The dielectric and electric polarization measurements were carried out in PPMS by using an inductance-capacitance-resistance (LCR) meter (E4980A, Agilent) and high-resistance current meter (6517B, Keithley), respectively. No electric-field poling procedure was carried out at the pyroelectric current measurement. Detailed information on the sample holder used for the electrical and magnetic measurements is presented in Fig. S2. The samples for all measurements are from the same batch. To make a comparison, the same sample from each composition was used for electric-field modulation of magnetization, dielectric, and electric polarization measurements.

III. RESULTS

Figure 1(a) shows the crystal structure of $Ni_{2-x}Fe_xMo_3O_8$. It is composed of Fe/Ni oxide layers and trimerized MoO_4 layers along the *c* axis, belonging to a polar space group $P6_3mc$ [29]. The honeycomb lattice is a bipartite lattice composed of two triangular sublattices from the direction of the *c* axis. Octahedrally and tetrahedrally coordinated Ni^{2+}/Fe^{2+} occupy these two triangular sublattices, respectively, as shown in Fig. 1(b). The previous Mössbauer study revealed that Fe atoms prefer to occupy the oxygen-coordinated tetrahedral site [33]. Figure 1(c) shows the x-ray-diffraction (XRD) patterns of the single crystal of $Ni_{2-x}Fe_xMo_3O_8$ ($x = 0$, 0.5, 1.0, 1.5, and 2.0) at room temperature. The diffraction peaks of $Ni_2Mo_3O_8$ from the *ab* plane are consistent with (00*l*) peaks in PDF No. 00–037–0855. The equally spaced 2θ values of (00*l*) are a typical single-crystal feature. Upon Fe doping, the individual peak positions of $Ni_{2-x}Fe_xMo_3O_8$ ($x = 0$, 0.5, 1.0, 1.5, and 2.0) gradually shift to lower angles. The XRD features reveal the increase of the *c*-axis lattice and systematic doping level of Fe^{2+} with the increasing *x*. The *c*-axis lattice parameters as a function of *x* are shown in Fig. S3.

TEM technique is used to gain insight into the crystal structure. A low-magnification high-angle annular dark-field (HAADF) image of the $NiFeMo_3O_8$ flake is shown in Fig. 2(a). The elemental mappings of $NiFeMo_3O_8$ obtained by EDS confirm the homogeneous distribution of chemical elements (Fe, Ni, Mo, and O), as shown in Figs. 2(b)–2(e).

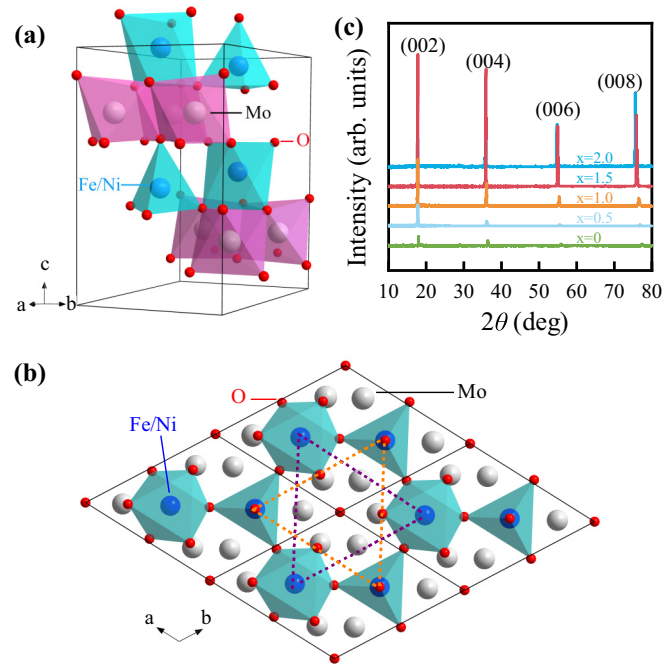

FIG. 1. (a) Crystal structure of $Ni_{2-x}Fe_xMo_3O_8$ with polar space group $P6_3mc$. (b) The crystal structure of $Ni_{2-x}Fe_xMo_3O_8$ viewed from the direction of *c* axis. The dashed lines highlight the octahedral and tetrahedral triangular sublattices. (c) The diffraction peaks of *ab* plane (00*l*) in $Ni_{2-x}Fe_xMo_3O_8$ ($x = 0$, 0.5, 1.0, 1.5, and 2.0).

Electron-diffraction patterns taken with [001] and [010] zone axis were detected as shown in Figs. 2(f) and 2(h). The corresponding HAADF images are shown in Figs. 2(g) and 2(i). Fe/Ni atoms and Mo atoms are marked with yellow solid circles and pink solid circles in Figs. 2(g) and 2(i), respectively, with the small hexagonal honeycomb composed of two layers of trimerized Mo atoms and the large hexagonal honeycomb composed of Fe/Ni atoms. With the obtained interplanar spacing of (100) and (002) planes as shown in Figs. 2(g) and 2(i), we can calculate the lattice constant of $a = d_{(100)}/\cos 30^\circ \approx 5.77$ Å and $c = 2 \times d_{(002)} \approx 10$ Å, which is consistent with the previous literature [34].

The magnetism of sample comes from unpaired 3*d* electrons in Ni^{2+}/Fe^{2+} ions, with no contribution from Mo^{4+} ion due to the formation of spin-singlet trimmers [35]. Previous research of magnetization and powder neutron diffraction on $Ni_2Mo_3O_8$ and $Fe_2Mo_3O_8$ illustrated that their antiferromagnetic ground states belong to the magnetic point group of $mm2$ [34] and $6'mm'$ [36], respectively. $Ni_2Mo_3O_8$ was an ordered magnetic state characterized as an admixture of stripy and zigzag AFM ordered magnetic state. Figure 3(a) shows zigzag spin lattice from *b*-direction components of $Ni_2Mo_3O_8$. The zigzag spin lattice belongs to geometrical spin frustration. Strong geometrical spin frustration suppresses the long-range magnetic ordering of the Néel state. In contrast, $Fe_2Mo_3O_8$ has collinear antiferromagnetic order, and the direction of the Fe spin is parallel to the *c* axis as presented in Fig. 3(b).

Figure 3(c) demonstrates the temperature (*T*) dependence of the magnetic susceptibility (χ) curve in $Ni_{2-x}Fe_xMo_3O_8$ ($x = 0$, 0.5, 1.0, and 1.5) after the field-cooling (FC) procedure with $H = 1$ kOe parallel to the *c* axis. The magnetization

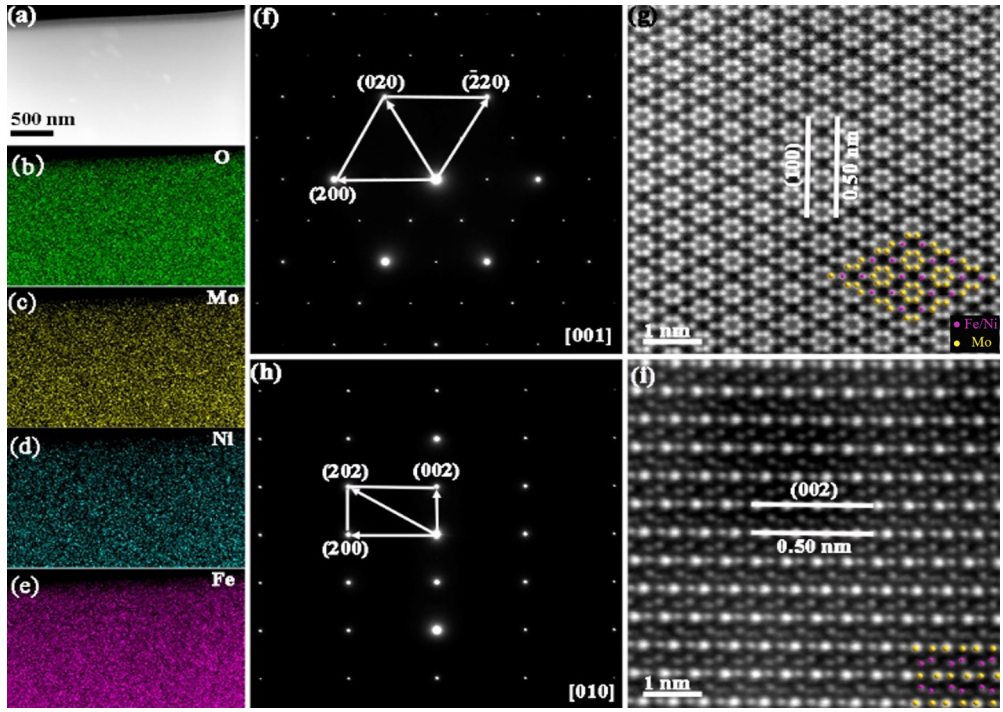

FIG. 2. (a) A low-magnification HAADF image of $NiFeMo_3O_8$ and the corresponding EDX elemental mapping of (b) O, (c) Mo, (d) Ni, and (e) Fe. Corresponding electron-diffraction pattern viewed from (f) [001] and (h) [010] zone axis. HADDF images of $NiFeMo_3O_8$ viewed along (g) the [001] and (i) [010] zone axis. The right corner of (g) and (i): the atomic model of $NiFeMo_3O_8$ overlaid on the top of HADDF images.

drop of the *M-T* curve for all compositions is a typical antiferromagnetic ordering characteristic. For $x = 0$, the antiferromagnetic transition temperature (T_N) of $Ni_2Mo_3O_8$ is 5 K, as highlighted by the arrow in the inset of Fig. 3(c). With the increase of Fe content, T_N gradually increases to 45 K ($x = 0.5$), 54.9 K ($x = 1.0$), and 60 K ($x = 1.5$), respectively. The $\chi^{-1}(T)$ curves are fitted by Curie-Weiss formula $\chi^{-1} = C/T - \theta$, where C is the Curie-Weiss constant and θ is referred to as the Curie-Weiss temperature. The obtained Curie-Weiss temperatures were -140.7 K ($x = 0$), -130.5 K ($x = 0.5$), -187.5 K ($x = 1.0$), and -331.4 K ($x = 1.5$), and negative values of θ indicate AFM interactions. To describe magnetic frustration, the frustration index $f(f = |\theta|/T_N)$ was introduced, where strong spin-frustration systems are thought to be those associated with $f > 5$ [37]. The frustration indices f for $Ni_2Mo_3O_8$ and $Ni_{0.5}Fe_{1.5}Mo_3O_8$ were 28 and 5.5, respectively, indicating strong magnetic frustration in $Ni_2Mo_3O_8$ and weak frustration in $Ni_{0.5}Fe_{1.5}Mo_3O_8$. For the sample of $x = 0.5$ and $x = 1.0$, the frustration index f falls in the range of 2–5 [2.8 ($x = 0.5$) and 3.4 ($x = 1.0$)], which are typically regarded as unfrustrated systems [38]. Figures S4(a)–S4(d) show the *M-T* curves of $Ni_{2-x}Fe_xMo_3O_8$ ($x = 0$, 0.5, 1.0, and 1.5) under different magnetic field. T_N shifts to lower temperature as magnetic field increases, indicating that magnetic field inhibits the formation of antiferromagnetic order. Figure 3(d) shows the specific-heat $C_p(T)$ curves of $Ni_{2-x}Fe_xMo_3O_8$ ($x = 0$, 0.5, 1.0, and 1.5). Typical λ-shaped anomalies were observed at 5 K ($x = 0$), 45 K ($x = 0.5$), 54.9 K ($x = 1.0$), and 60 K ($x = 1.5$), respectively. The linear behavior of C_p/T^2 vs T plot of $Ni_2Mo_3O_8$ signifies the typical antiferromagnetic behavior in the low-temperature region in Fig. S5.

The magnetic-field dependence of magnetization under $H \parallel c$ for different samples were measured at various temperatures. For low Fe-doping levels of $x = 0.5$ and $x = 1.0$, the typical linear *M-H* curves representing antiferromagnetic behavior were observed up to $\mu_0 H = 9$ T as shown in Fig. S6. As for the higher Fe-doping level of $x = 1.5$ as shown in Fig. 3(f), a slight deviation from the linear dependence occurs at 28.6 kOe (defined as H_{cri}) when $T = 59$ K. This deviation reflects the spin flop transition-induced metamagnetic state. With the decrease of temperature, H_{cri} moves to a higher magnetic field as shown in Fig. 3(f). From above, we can see that a higher Fe-doping level can induce the spin flop transition, which may be due to the modification of magnetic interactions.

Figure 4(a) shows the temperature dependence of the relative dielectric constant [$\Delta\varepsilon = \varepsilon(T) - \varepsilon(30\,\mathrm{K})$] of $Ni_{2-x}Fe_xMo_3O_8$ ($x = 0$, 0.5, 1.0, and 1.5) under zero magnetic field. For $x = 0$, the peak on the dielectric curve was observed at 5 K (defined as T_1). Upon Fe doping, the dielectric anomalies occur at 45 K ($x = 0.5$), 54.5 K ($x = 1.0$), and 60.3 K ($x = 1.5$), respectively, corresponding well to T_N, indicating the magnetoelectric coupling effect in $Ni_{2-x}Fe_xMo_3O_8$. Figures S7(a), S7(d), and S7(g) show the ε-*T* curves of $Ni_{2-x}Fe_xMo_3O_8$ ($x = 0.5$, 1.0, and 1.5) with different magnetic fields, and the dielectric anomalies T_1 in ε-*T* curves are sorted out in Fig. 4(b). T_1 shifts to a lower temperature with increasing magnetic field, consistent with T_N response to H. To gain insight into the dielectric anomaly at T_1, pyroelectricity of $Ni_{2-x}Fe_xMo_3O_8$ ($x = 0$, 0.5, 1.0, and 1.5) was studied as shown in Fig. 4(c), where the electric polarization was obtained by integrating the pyroelectric current

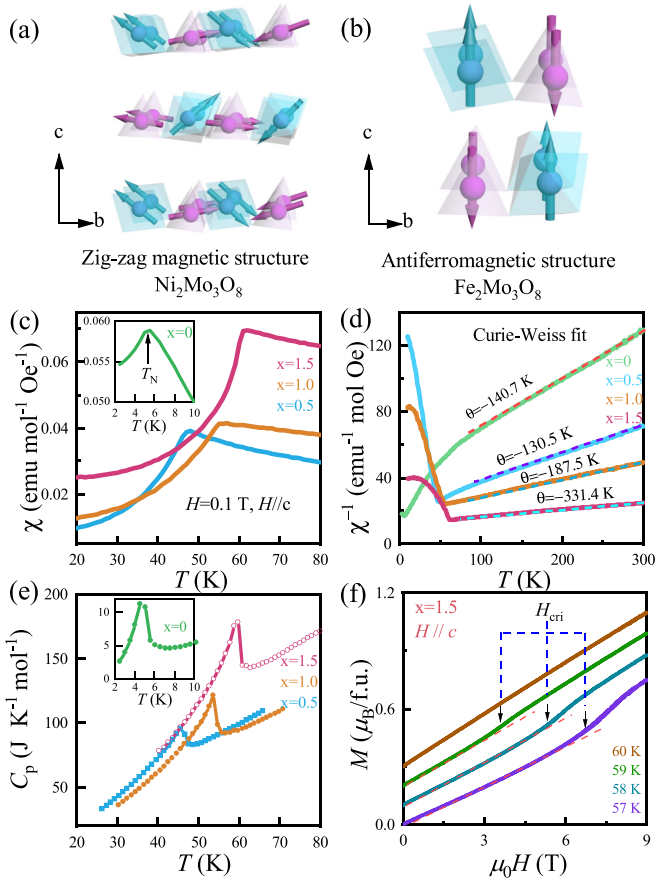

FIG. 3. (a) Zigzag magnetic structure from *b*-direction components of the $Ni_2Mo_3O_8$. (b) Collinear antiferromagnetic order of $Fe_2Mo_3O_8$ (c) Temperature dependence of magnetic susceptibility (χ) for $Ni_{2-x}Fe_xMo_3O_8$ ($x = 0$, 0.5, 1.0, and 1.5) with a magnetic field of 0.1 T after field cooling (FC) under $H \parallel c$. (d) Temperature dependence of inverse magnetic susceptibility χ^{-1} measured along the *c* axis. The dashed lines are fitting curve by Curie-Weiss equation. (e) Heat capacity vs temperature plot of $Ni_{2-x}Fe_xMo_3O_8$ ($x = 0$, 0.5, 1.0, and 1.5). (f) The magnetic-field dependence of magnetization measured at selected temperatures for $Ni_{0.5}Fe_{1.5}Mo_3O_8$.

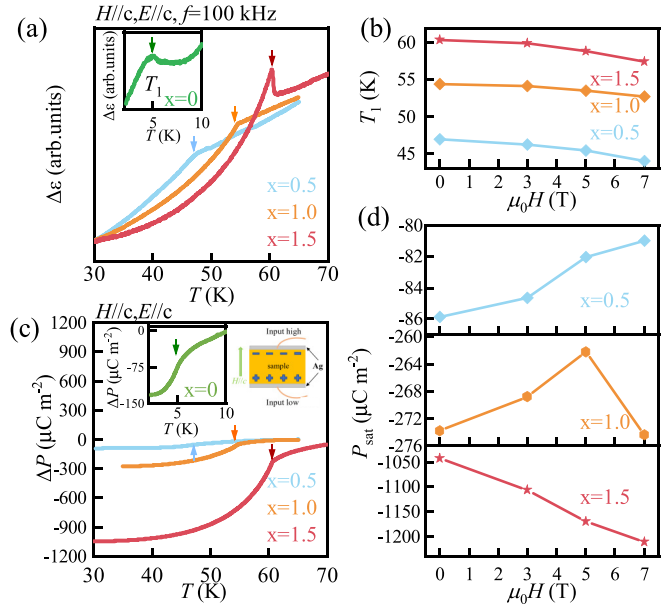

FIG. 4. (a) Temperature dependence of relative dielectric constant $\Delta\varepsilon$ [$\Delta\varepsilon = \varepsilon(T)$–$\varepsilon(30\,\mathrm{K})$] for $Ni_{2-x}Fe_xMo_3O_8$ ($x = 0$, 0.5, 1.0, and 1.5). (b) The magnetic-field dependence of the dielectric anomalous temperature (T_1) for $Ni_{2-x}Fe_xMo_3O_8$ ($x = 0.5$, 1.0, and 1.5). (c) Electric polarization (ΔP) as a function of T for $Ni_{2-x}Fe_xMo_3O_8$ ($x = 0$, 0.5, 1.0, and 1.5). (d) The magnetic-field dependence of the saturated polarization (P_{sat}) for $Ni_{2-x}Fe_xMo_3O_8$ ($x = 0.5$, 1.0, and 1.5).

with time. For $x = 0$, as temperature approaches T_N (T_1), a steep drop occurs on P-T curve and P gradually reaches the saturated value of $-133\,\mu\mathrm{C\,m^{-2}}$ at low temperature. With the increase of Fe content, net P of $Ni_{2-x}Fe_xMo_3O_8$ ($x = 0.5$, 1.0, and 1.5) also appears at T_N (T_1), and saturated polarizations are $-85.8\,\mu\mathrm{C\,m^{-2}}$ ($x = 0.5$), $-273.8\,\mu\mathrm{C\,m^{-2}}$ ($x = 1.0$), and $-1041.6\,\mu\mathrm{C\,m^{-2}}$ ($x = 1.5$), respectively. The above results indicate that the magnetic transition is accompanied with the modulation of electric polarization along the *c* axis, and the electric polarization is greatly enhanced as the amount of doped Fe content increases. Subsequently, ΔP-T curves of $Ni_{2-x}Fe_xMo_3O_8$ ($x = 0.5$, 1.0, and 1.5) were measured under different magnetic fields as presented in Figs. S7(c), S7(f), and S7(i) and Fig. 4(d), which presents the magnetic-field modulation of electric polarization.

ε-H and ΔP-H curves were measured at different temperatures with $H \parallel c$ axis to further study the magnetoelectric properties in $Ni_{2-x}Fe_xMo_3O_8$ ($x = 0.5$, 1.0, and 1.5). As shown in Figs. S8(a), S8(d), and S8(g), the magnetodielectric curves show linear behavior when the temperature is above T_N, presenting no hint of magnetoelectric effect. In contrast, when the temperature is lower than T_N, for $x = 0.5$ and 1.0, the dielectric constant is quadratically changed with magnetic field. Moreover, when $x = 1.5$, the magnetodielectric curve presents anomalies at $H = 28.6$ and -27.8 kOe marked by black arrow at $T = 59$ K as shown in Fig. 5(a). Magnetodielectric peaks become sharp and gradually shift to a high magnetic field with temperature decreasing in Fig. 5(b). The onset H of dielectric anomaly is consistent with the phase boundary of AFM and spin flop (SF) on M/H-H curves as demonstrated in Fig. 5(c), which indicates that the dielectric behavior is associated with the spin flop transition.

To confirm the ME effect, the ME current density(J) was collected by sweeping the magnetic field at various temperature, as shown in Figs. S8(b), S8(e), and S8(h). The calculated variation of polarization data $\Delta P(H)$ is plotted in Fig. 5(d). For $x = 0.5$ and 1.0, the ΔP-H curves followed a parabolic behavior in the AFM region. In contrast, for sample $x = 1.5$ at $T = 59$ K, the ΔP-H curve followed a parabolic behavior in the AFM region and ΔP linearly changed with H in SF phase. With the temperature decreases, the onset field (parabolic to linear ΔP-H) gradually shifted to a higher magnetic field and ΔP ($H = 70$ kOe) gradually increased, as shown in Fig. 5(e). To present a quantitative evaluation of the ME effect, the ME coefficients were obtained by fitting the positive magnetic-field region of ΔP-H curve using a polynominal equation $\Delta P = \alpha H + \beta H^2$, where α and β are the first-order and second-order ME coefficients,

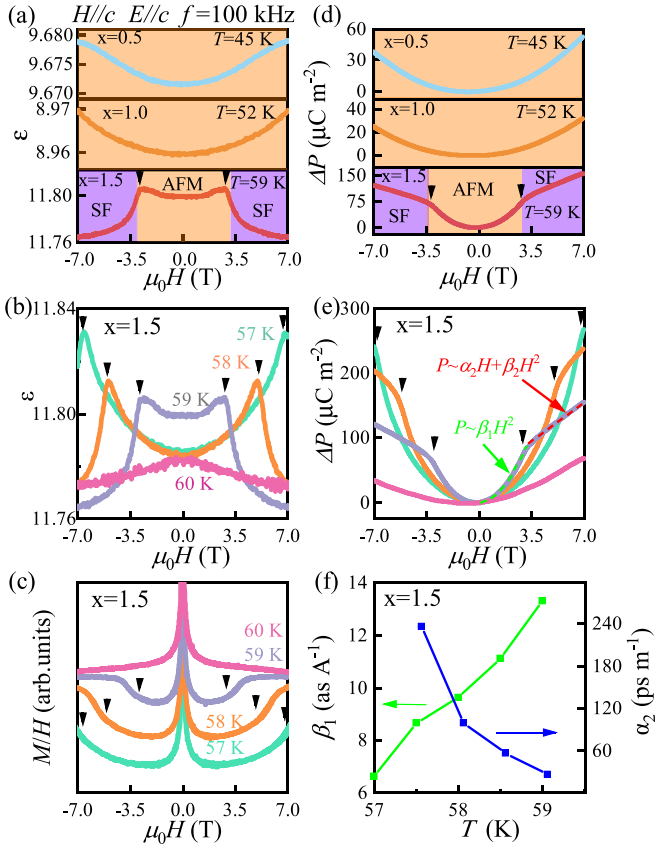

FIG. 5. The magnetic-field dependence of (a) relative dielectric constant (ε) and (d) relative electric polarization(ΔP) for $Ni_{2-x}Fe_xMo_3O_8$ ($x = 0.5$, 1.0, and 1.5) at 45, 52, and 59 K, respectively. The magnetic-field dependence of (b) ε, (c) M/H, and (e) ΔP at 57, 58, 59, and 60 K for $Ni_{0.5}Fe_{1.5}Mo_3O_8$. The dashed bright-green line and dashed red curve are the fits to the ΔP-H curve with the different functions of $\Delta P \sim \beta_1 H^2$ and $\Delta P = \alpha_2 H + \beta_2 H^2$, where α_2, β_1, and β_2 are constants. The SF transition points are marked by a black arrow. (f) The temperature dependence of β_1 and α_2 for $Ni_{0.5}Fe_{1.5}Mo_3O_8$.

respectively. The $\Delta P(H)$ curves in the AFM region showed perfect quadratic fittings to the magnetic field ($\Delta P = \beta_1 H^2$), as illustrated by the dashed bright-green curve in Fig. 5(e). β_1 (59 K) was $\sim 13 \times 10^{-18}$ s A^{-1}, which is larger than those found for $Ni_2Mo_3O_8$ (5.1×10^{-18} s A^{-1}) [30], $Fe_2Mo_3O_8$ (1.81×10^{-28} s A^{-1}) [25], and $Co_2Mo_3O_8$ (2.9×10^{-18} s A^{-1}) [39]. β_1 decreased as the temperature was reduced, as shown in Fig. 5(f). The data in the SF region were well fitted by $\Delta P = \alpha_2 H + \beta_2 H^2$, as denoted by the dashed pink curve. α_2 (59 K) was about 30 ps m^{-1}, and α_2 increased as the temperature decreased. When $T = 57.5$ K, α_2 was 238 ps m^{-1}, which was much larger than those typical linear ME materials, including Cr_2O_3 ($\sim$4.13 ps m^{-1}) [40], $Ni_2Mo_3O_8$($\sim$70 ps m^{-1}) [30], $Fe_2Mo_3O_8$ (differential ME coefficient $\sim 10^4$ ps m^{-1} at transition boundary and linear part of ME coefficient ~ -16.2 ps m^{-1} at the ferrimagnetic region) [23,26], and Fe_3O_4 ($\sim$50 ps m^{-1}) [41].

The magnetization was performed under electric field to study the converse magnetoelectric effect. Figures 6(a)–6(c) show the magnetization periodically modulated with a continuous electric field at 7 T for $Ni_{2-x}Fe_xMo_3O_8$ ($x = 0.5$,

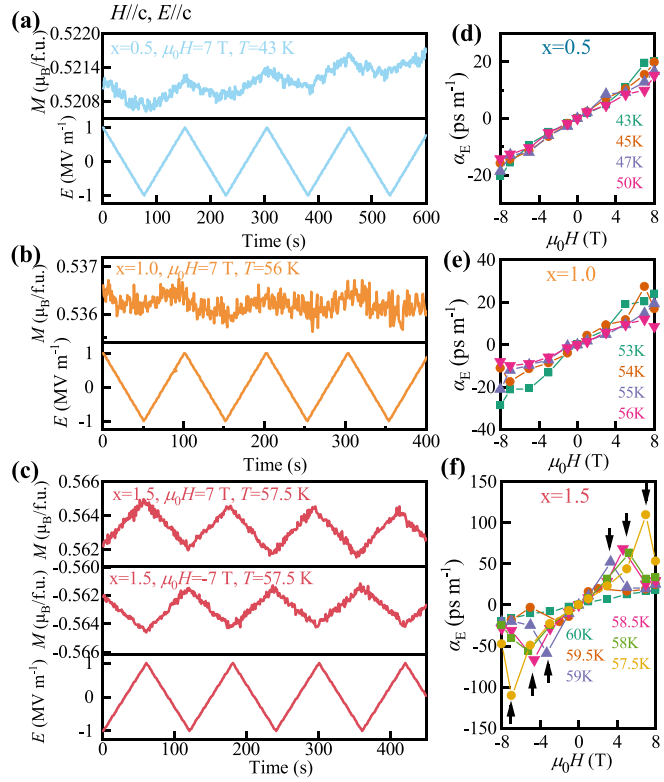

FIG. 6. The periodical modulation of magnetization as a function of time for $Ni_{2-x}Fe_xMo_3O_8$ [x = (a) 0.5, (b) 1.0, and (c) 1.5] at selected temperature. The magnetic-field dependence of inverse ME coefficient(α_E) at various temperatures for $Ni_{2-x}Fe_xMo_3O_8$ [x = (d) 0.5, (e) 1.0, and (f) 1.5]. The SF transition points are marked by a black arrow.

1.0, and 1.5) with $H \parallel E \parallel c$-axis configuration, where M almost linearly changes with E. In contrast, the trend of M changing with E reverses when $\mu_0 H$ is reversed to -7 T. M-E curves were also measured at other temperature and different bias H. The converse ME coefficients (α_E) are obtained by fitting the quadratic equation: $\mu_0 M(E, H) = \alpha_E E + \beta_E E^2 + \mu_0 M(0, H)$, where $M(E, H)$ is the average of the increasing and decreasing E-scan data, and α_E and β_E are the first-order and second-order converse ME coefficients, respectively. Notably, the linear term α_E was dominated and α_E were sorted out as shown in Figs. 6(d)–6(f). As for $x = 0.5$ and 1.0, α_E increased with the magnetic field increasing. The maximum α_E is 20 ps m^{-1} (43 K, $x = 0.5$) and 28 ps m^{-1} (53 K, $x = 1.0$) at 8 T, respectively. For $x = 1.5$, the maximum α_E marked by black arrows was achieved at the boundary of AFM-SF phase at each temperature, and the highest α_E was achieved at $T = 57.5$ K, with $H = 7$ T with $\alpha_E = 110$ ps m^{-1}. Furthermore, the magnetization modulation under sequential square electric-field waves was also measured in $Ni_{0.5}Fe_{1.5}Mo_3O_8$ at 57.5 K. M reacts rapidly under 7 T when the sample is applied to continuous electric field of 1, 0. and -1 MV m^{-1}. In contrast, when the sign of H is reversed, E-induced high or low state of M is also reversed, as shown in Fig. S9 [31].

IV. DISCUSSION

All measured data were adequate to draft the H-T phase diagram for each composition, as shown in Figs. 7(a)–7(d),

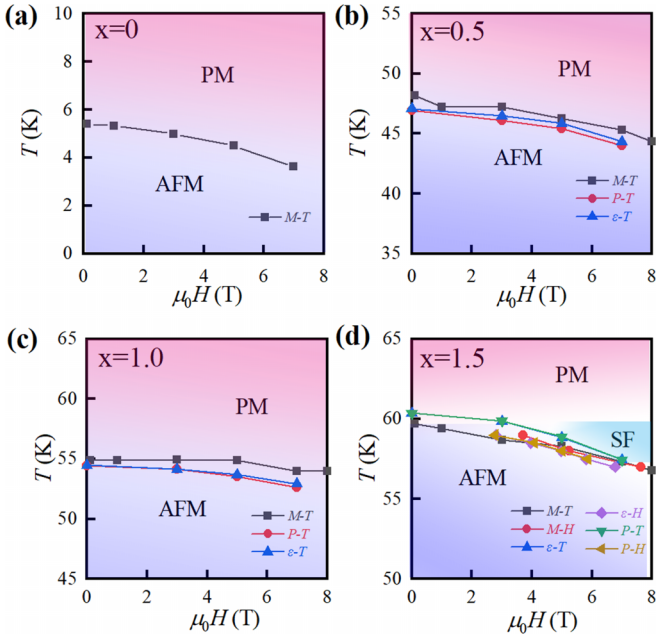

FIG. 7. (a)–(d) The *H*-*T* phase diagrams for $Ni_{2-x}Fe_xMo_3O_8$ ($x = 0$, 0.5, 1.0, and 1.5) under $H \parallel c$, as decided by magnetization, polarization, and dielectric measurements. PM, AFM, and SF indicate paramagnetic, antiferromagnetic, and spin flop phase, respectively.

respectively. The phase regions are determined by the peak position in the $M(T)$, $M(H)$, $P(T)$, $\Delta P(H)$, $\varepsilon(T)$, and $\varepsilon(H)$. As for $x = 0$, 0.5, and $x = 1.0$, the AFM ground state is separated from the paramagnetic (PM) phase by the AFM Néel point T_N and T_1 in different magnetic fields. For $x = 1.5$, when $T < 60$ K and magnetic field exceeds H_{cri}, SF phase appears. However, for low doping content of Fe, H_{cri} may appear at higher magnetic field, which cannot be observed in our experiment. There are no sufficient experiments to clarify the magnetic phase at this stage and ME responses of a comprehensive origination are discussed below.

$Ni_2Mo_3O_8$ has a ground state of specific noncollinear magnetic structure and $Fe_2Mo_3O_8$ belongs to the collinear spin order. It is possible that Fe-doped $Ni_2Mo_3O_8$ induces a noncollinear magnetic structure due to the competing magnetic interactions, especially for $Fe_{0.5}Ni_{1.5}Mo_3O_8$ with the magnetic frustration index of 5.5. Under this circumstance, we cannot exclude the ME origination from inverse Dzyaloshinskii-Moriya (IDM) interaction [$P \propto e_{12} \times (S_1 \times S_2)$, where S_1 and S_2 are the neighboring spins, and e_{12} denotes the connection from S_1 and S_2]. However, in our measurements, the IDM mechanism does not contribute to the polarization due to the $H \parallel P \parallel c$ relation. The *d*-*p* hybridization [$P \propto e_1 \times (e_1 S_1)^2$, where e_1 denotes the vector between transition metal and its ligand atoms] depending on the spin configuration has no fixed relationship of P and H. $Fe_2Mo_3O_8$ cancel P with respect to the c axis due to the collinear AFM structure, and $Ni_2Mo_3O_8$ can give rise to nonzero polarization because of noncollinear arrangement of Ni [25,30]. In our case, *d*-*p* hybridization can produce electric polarization along the c axis with specific spin configuration in Fe-doped $Ni_{2-x}Fe_xMo_3O_8$. However, the inverse DM interaction and *d*-*p* hybridization mechanism are both from spin-orbital coupling effect. Moreover, the nonrelativistic exchange striction mechanism described by $P \propto e_{12}(S_1 S_2)$ supports that the electric polarization along the c axis in $Ni_{2-x}Fe_xMo_3O_8$ may be due to the collinear magnetic moment component. Different from the tremendous P jump in $Fe_2Mo_3O_8$ at H_{cri} (collinear AFM to ferrimagnetic), the slight change of P for $Fe_{1.5}Ni_{0.5}Mo_3O_8$ occurs at H_{cri}, which may be due to the minor exchange energy gain (AFM to SF). Additionally, the magnetic point group for the antiferromagnetic order is $6'mm'$ in $Fe_2Mo_3O_8$, allowing the second-order ME effect. It possesses the symmetry element necessary to produce piezomagnetic effect [42], which may also apply to $Ni_{0.5}Fe_{1.5}Mo_3O_8$. In this way, the magnetostriction effect (spin-lattice coupling) may also play a role in $Ni_{0.5}Fe_{1.5}Mo_3O_8$ under a magnetic field due to the doped magnetic ion (Fe^{2+})-induced elongation of FeO_4 tetrahedron and possible change of spin state [43,44]. This occurrence further enhances the linear ME effect of $Ni_{0.5}Fe_{1.5}Mo_3O_8$.

V. CONCLUSION

By substituting the magnetic ion in $Ni_2Mo_3O_8$, the primary structural characteristics remain intact. However, with the increase of Fe content, the antiferromagnetic temperature was improved, antiferromagnetic exchange interaction was enhanced, and the magnetic field of spin flop transition decreased; the influence of the magnetic field on the spontaneous ferroelectric polarization associated with the specific AFM ordering gradually changed from inhibition to promotion. The clear magnetism-driven ferroelectricity behaviors have been demonstrated by the quadratic ME response in the AFM region and linear ME response in the SF region. Significant tunability of linear ME and converse ME effect was achieved due to the delicate modification of magnetic interactions. Overall, Fe chemical doping control is an effective method to achieve the modification of magnetoelectric materials in the frustrated magnet $Ni_2Mo_3O_8$.

ACKNOWLEDGMENTS

This work was financially by the National Natural Science Foundation of China (Grants No. 52272127 and No. U21A201910), the Research Program of the College Science & Technology of Hebei Province (Grant No. BJ2020013), the Hebei Natural Science Foundation (Grant No. E2023203002), and the Jiangsu Funding Program for Excellent Postdoctoral Talent.

The authors declare no competing financial interest.

[1] T. Kimura, T. Goto, H. Shintani, K. Ishizaka, T. Arima, and Y. Tokura, Magnetic control of ferroelectric polarization, Nature (London) **426**, 55 (2003).

[2] S. Dong, J.-M. Liu, S.-W. Cheong, and Z. Ren, Multiferroic materials and magnetoelectric physics: Symmetry, entanglement, excitation, and topology, Adv. Phys. **64**, 519 (2015).

[3] M. Fiebig, T. Lottermoser, D. Meier, and M. Trassin, The evolution of multiferroics, Nat. Rev. Mater. **1**, 16046 (2016).

[4] K. Zhai, D.-S. Shang, Y.-S. Chai, G. Li, J.-W. Cai, B.-G. Shen, and Y. Sun, Room-temperature nonvolatile memory based on a single-phase multiferroic hexaferrite, Adv. Funct. Mater. **28**, 1705771 (2018).

[5] S. Zhao, Z. Zhou, C. Li, B. Peng, Z. Hu, and M. Liu, Low-voltage control of $(Co/Pt)_x$ perpendicular magnetic anisotropy heterostructure for flexible spintronics, ACS Nano **12**, 7167 (2018).

[6] A. Chen, Y. Wen, B. Fang, Y. Zhao, Q. Zhang, Y. Chang, P. Li, H. Wu, H. Huang, Y. Lu, Z. Zeng, J. Cai, X. Han, T. Wu, X.-X. Zhang, and Y. Zhao, Giant nonvolatile manipulation of magnetoresistance in magnetic tunnel junctions by electric fields via magnetoelectric coupling, Nat. Commun. **10**, 243 (2019).

[7] Z. Chu, C. Dong, C. Tu, X. Liang, H. Chen, C. Sun, Z. Yu, S. Dong, and N.-X. Sun, A low-power and high-sensitivity magnetic field sensor based on converse magnetoelectric effect, Appl. Phys. Lett. **115**, 162901 (2019).

[8] C. Lu, M. Wu, L. Lin, and J.-M. Liu, Single-phase multiferroics: New materials, phenomena, and physics, Natl. Sci. Rev. **6**, 653 (2019).

[9] N. A. Spaldin and R. Ramesh, Advances in magnetoelectric multiferroics, Nat. Mater. **18**, 203 (2019).

[10] S. Bao, W. Wang, Y. Y. Shangguan, Z. W. Cai, Z. Y. Dong, Z. T. Huang, W. Si, Z. Ma, R. Kajimoto, K. Ikeuchi, S. Yano, S. L. Yu, X. G. Wan, J. .X. Li, and J. S. Wen, Neutron spectroscopy evidence on the dual nature of magnetic excitations in a van der Waals metallic ferromagnet $Fe_{2.72}GeTe_2$, Phys. Rev. X **12**, 011022 (2022).

[11] Y. Tokura, S. Seki, and N. Nagaosa, Multiferroics of spin origin, Rep. Prog. Phys. **77**, 076501 (2014).

[12] H. Katsura, N. Nagaosa, and A. V. Balatsky, Spin current and magnetoelectric effect in noncollinear magnets, Phys. Rev. Lett. **95**, 057205 (2005).

[13] H. Murakawa, Y. Onose, S. Miyahara, N. Furukawa, and Y. Tokura, Ferroelectricity induced by spin-dependent metal-ligand hybridization in $Ba_2CoGe_2O_7$, Phys. Rev. Lett. **105**, 137202 (2010).

[14] J. T. Haraldsen, F. Ye, R. S. Fishman, J. A. Fernandez-Baca, Y. Yamaguchi, K. Kimura, and T. Kimura, Multiferroic phase of doped delafossite $CuFeO_2$ identified using inelastic neutron scattering, Phys. Rev. B **82**, 020404(R) (2010).

[15] T.-h. Arima, Ferroelectricity induced by proper-screw type magnetic order, J. Phys. Soc. Jpn. **76**, 073702 (2007).

[16] N. Lee, Y. J. Choi, M. Ramazanoglu, W. Ratcliff, V. Kiryukhin, and S. W. Cheong, Mechanism of exchange striction of ferroelectricity in multiferroic orthorhombic $HoMnO_3$ single crystals, Phys. Rev. B **84**, 020101(R) (2011).

[17] S. Picozzi, K. Yamauchi, B. Sanyal, I. A. Sergienko, and E. Dagotto, Dual nature of improper ferroelectricity in a magnetoelectric multiferroic, Phys. Rev. Lett. **99**, 227201 (2007).

[18] Y. J. Choi, H. T. Yi, S. Lee, Q. Huang, V. Kiryukhin, and S. W. Cheong, Ferroelectricity in an Ising chain magnet, Phys. Rev. Lett. **100**, 047601 (2008).

[19] J. W. Kim, S. Artyukhin, E. D. Mun, M. Jaime, N. Harrison, A. Hansen, J. J. Yang, Y. S. Oh, D. Vanderbilt, V. S. Zapf, and S. W. Cheong, Successive magnetic-field-induced transitions and colossal magnetoelectric effect in Ni_3TeO_6, Phys. Rev. Lett. **115**, 137201 (2015).

[20] J. Wang, M. Tokunaga, Z. Z. He, J. I. Yamaura, A. Matsuo, and K. Kindo, High magnetic field induced phases and half-magnetization plateau in the $S = 1$ kagome compound $Ni_3V_2O_8$, Phys. Rev. B **84**, 220407(R) (2011).

[21] J. C. T. Lee, S. Yuan, S. Lal, Y. I. Joe, Y. Gan, S. Smadici, K. Finkelstein, Y. Feng, A. Rusydi, P. M. Goldbart, S. L. Cooper, and P. Abbamonte, Two-stage orbital order and dynamical spin frustration in $KCuF_3$, Nat. Phys. **8**, 63 (2012).

[22] L. H. Yin, Y. M. Zou, J. Yang, J. M. Dai, W. H. Song, X. B. Zhu, and Y. P. Sun, Colossal magnetodielectric effect and spin flop in magnetoelectric $Co_4Nb_2O_9$ crystal, Appl. Phys. Lett. **109**, 032905 (2016).

[23] Y. Wang, G. L. Pascut, B. Gao, T. A. Tyson, K. Haule, V. Kiryukhin, and S.-W. Cheong, Unveiling hidden ferrimagnetism and giant magnetoelectricity in polar magnet $Fe_2Mo_3O_8$, Sci. Rep. **5**, 12268 (2015).

[24] N. Abe, N. D. Khanh, T. Sasaki, and T. Arima, Magnetic-field-induced spin flop transition and magnetoelectric effect in $Ca_2Fe_{2-x}Al_xO_5$, Phys. Rev. B **89**, 054437 (2014).

[25] T. Kurumaji, S. Ishiwata, and Y. Tokura, Doping-tunable ferrimagnetic phase with large linear magnetoelectric effect in a polar magnet $Fe_2Mo_3O_8$, Phys. Rev. X **5**, 031034 (2015).

[26] S. Nakayama, R. Nakamura, M. Akaki, D. Akahoshi, and H. Kuwahara, Ferromagnetic behavior of $(Fe_{1-y}Zn_y)_2Mo_3O_8$ $(0 \leqslant y \leqslant 1)$ induced by nonmagnetic Zn substitution, J. Phys. Soc. Jpn. **80**, 104706 (2011).

[27] T. Kurumaji, S. Ishiwata, and Y. Tokura, Diagonal magnetoelectric susceptibility and effect of Fe doping in the polar ferrimagnet $Mn_2Mo_3O_8$, Phys. Rev. B **95**, 045142 (2017).

[28] J. K. Yang, D. Su, J. C. He, Y. Ji, Q. W. Guo, Y. Meng, X. F. Li, L. Y. Wang, X. Shen, Y. Yao, Y. W. Long, Y. Sun, and R. C. Yu, Mg doping enhanced magnetoelectric effect in the polar magnet $Fe_2Mo_3O_8$, Phys. Rev. B **107**, 104408 (2023).

[29] J. R. Morey, A. Scheie, J. P. Sheckelton, C. M. Brown, and T. M. McQueen, $Ni_2Mo_3O_8$: Complex antiferromagnetic order on a honeycomb lattice, Phys. Rev. Mater. **3**, 014410 (2019).

[30] Y. S. Tang, J. H. Zhang, L. Lin, R. Chen, J. F. Wang, S. H. Zheng, C. Li, Y. Y. Zhang, G. Z. Zhou, L. Huang, Z. B. Yan, X. M. Lu, D. Wu, X. K. Huang, X. P. Jiang, and J. M. Liu, Metamagnetic transitions and magnetoelectricity in the spin-1 honeycomb antiferromagnet $Ni_2Mo_3O_8$, Phys. Rev. B **103**, 014112 (2021).

[31] See Supplemental Material at http://link.aps.org/supplemental/10.1103/PhysRevB.109.024442 for an additional the growth process of single crystal, the sample holder and physical properties characterization.

[32] P. Strobel and Y. Le Page, Growth and morphology of single crystals of hexagonal molybdates(IV) $M_2Mo_3O_8$ (M = Mn, Fe, Co, Ni), J. Cryst. Growth **61**, 329 (1983).

[33] F. Varret, H. Czeskleba, F. Hartmann-Boutron, and P. Imbert, Étude par effet Mössbauer de l'ion Fe^{2+} en symétrie trigonale dans les composés du type $(Fe, M)_2Mo_3O_8$ (M = Mg, Zn, Mn, Co, Ni) et propriétés magnétiques de $(Fe, Zn)_2Mo_3O_8$, J. Phys. France **33**, 549 (1972).

[34] S. P. McAlister and P. Strobel, Magnetic order in $M_2Mo_3O_8$ single crystals (M = Mn, Fe, Co, Ni), J. Magn. Magn. Mater. **30**, 340 (1983).

[35] F. A. Cotton, Metal atom clusters in oxide systems, Inorg. Chem. **3**, 1217 (1964).

[36] D. Bertrand and H. Kerner-Czeskleba, Étude structurale et magnétique de molybdates d'éléments de transition, J. Phys. France **36**, 379 (1975).

[37] A. Otsuka, D. V. Konarev, R. N. Lyubovskaya, S. S. Khasanov, M. Maesato, Y. Yoshida, and G. Saito, Design of spin-frustrated monomer-type $C_{60}^{\bullet}$ Mott insulator, Crystals **8**, 115 (2018).

[38] S. Mugiraneza and A. M. Hallas, Tutorial: A beginner's guide to interpreting magnetic susceptibility data with the Curie-Weiss law, Commun. Phys. **5**, 95 (2022).

[39] Y. S. Tang, S. M. Wang, L. Lin, C. Li, S. H. Zheng, C. F. Li, J. H. Zhang, Z. B. Yan, X. P. Jiang, and J. M. Liu, Collinear magnetic structure and multiferroicity in the polar magnet $Co_2Mo_3O_8$, Phys. Rev. B **100**, 134112 (2019).

[40] H. Wiegelmann, A. G. M. Jansen, P. Wyder, J. P. Rivera, and H. Schmid, Magnetoelectric effect of Cr_2O_3 in strong static magnetic fields, Ferroelectrics **162**, 141 (1994).

[41] G. T. Rado and J. M. Ferrari, Linear and bilinear magnetoelectric effects in magnetically biased magnetite Fe_3O_4, Phys. Rev. B **15**, 290 (1977).

[42] R. E. Newnham, *Properties of Materials: Anisotropy, Symmetry, Structure* (Oxford University Press, Oxford, 2004).

[43] S. Reschke, A. A. Tsirlin, N. Khan, L. Prodan, V. Tsurkan, I. Kézsmárki, and J. Deisenhofer, Structure, phonons, and orbital degrees of freedom in $Fe_2Mo_3O_8$, Phys. Rev. B **102**, 094307 (2020).

[44] C. Zhang, Y. Zhao, H. Nie, C. Zheng, F. Li, D. Zhou, R. Gao, H. Shen, S. Jiang, L. Zhang, and J. Sun, Significant structure modulation in polar antiferromagnet $FeCoMo_3O_8$, Phys. Status Solidi B **260**, 2200558 (2023).